OPTICS

Photonic arbitrary Chern vectors

Xiang Xi[1,2]†, Linyun Yang[3]†, Ziyao Wang[2]†, Bei Yan[4]†, Jing-Ming Chen[2]†, Yan Meng[1], Zhen-Xiao Zhu[2], Tao Xiao[2], Min-Qi Cheng[2], Zebin Zhu[2], Gui-Geng Liu[5], Hongcheng Wang[1], Xiankai Sun[6], Zhen Gao[2]*

The hallmark feature of three-dimensional (3D) Chern insulators is the topological Chern vector, $\mathbf{C} = (C_1, C_2, C_3)$, which extends the celebrated Chern-type bulk-edge correspondence from 2D to 3D systems. However, topological Chern vectors have thus far been limited to the simplest form with a single nonzero component, $\mathbf{C} = (0, 0, C_3)$, which restricts chiral surface states to appear only on four side surfaces with nonchiral transport along the direction of the Chern vector. Here, we theoretically propose and experimentally realize a 3D photonic Chern insulator with a Chern vector $\mathbf{C} = (1, 1, -1)$ in a tilted gyromagnetic photonic crystal. Its multiple nonzero components enable chiral surface states on all six crystal surfaces, exhibiting genuine chiral transport in arbitrary directions and nonreciprocal topological negative or positive refraction at the hinges. Furthermore, we demonstrate that arbitrary Chern vectors can be achieved via supercell modulation, enabling multimodal transport of chiral and torus knot or link surface states within a single crystal. This work establishes a comprehensive framework for topological Chern vectors and opens possibilities for nonreciprocal photonic devices.

INTRODUCTION

The discovery of photonic Chern insulators (*1*, *2*), characterized by a scalar Chern number and chiral edge states, has expanded the concept of topological phases of matter from fermions (electrons) to bosons (photons), giving rise to the field of topological photonics and enabling robust manipulations of electromagnetic waves with promising applications in topological waveguides (*3*–*12*), cavities (*13*–*17*), isolator (*18*), and laser (*19*). Recently, the concept of photonic Chern insulators has been extended from two-dimensional (2D) to 3D systems, accompanied by the generalization of the scalar Chern number C to a topological Chern vector $\mathbf{C} = (C_1, C_2, C_3)$ (*20*–*22*). The multicomponent and vectorial nature of topological Chern vectors leads to the generalization of Chern-type bulk-edge correspondence from 1D boundaries (chiral edge states) to 2D surfaces (chiral surface states), opening an avenue for exploring novel topological phenomena and designing nonreciprocal photonics devices, such as antichiral surface states (*23*), chiral hinge states (*24*–*28*), copropagating chiral zero modes (*29*), and 3D large-volume nonreciprocal transport (*30*).

However, to date, studies of 3D photonic Chern insulators have been restricted to the simplest form with only a single nonzero component, $\mathbf{C} = (0, 0, C_3)$. This limitation poses several critical problems, as schematically illustrated in Fig. 1A. First, the chiral surface states reside only on four side surfaces parallel to the Chern vector (purple arrow) rather than on all six surfaces. Second, the chiral surface states exhibit chiral (nonchiral) transport along the directions perpendicular (parallel) to the Chern vector, leading to weak topological protection and serious scattering loss when encountering a defect. Third, exotic phenomena such as torus knot or link surface states emerge only at the interface between two 3D Chern insulators with perpendicular Chern vectors rather than on a single crystal surface. To overcome these limitations, recent theoretical breakthroughs (*31*–*33*) have proposed the concept of arbitrary Chern vectors, $\mathbf{C} = (C_1, C_2, C_3)$. The presence of multiple nonzero components is predicted to yield richer chiral transport phenomena and more versatile applications. However, the experimental realization of arbitrary Chern vectors has remained elusive across all physical platforms to date.

Here, we report the first theoretical and experimental realization of a 3D photonic Chern insulator with a Chern vector $\mathbf{C} = (1, 1, -1)$ in a tilted gyromagnetic photonic crystal. In contrast to the previous 3D photonic Chern insulator limited to $\mathbf{C} = (0, 0, -1)$ (*22*), our $\mathbf{C} = (1, 1, -1)$ phase supports all-surface chiral surface states with genuine robust chiral transport along arbitrary directions, as illustrated in Fig. 1B. Moreover, we show that nonreciprocal and reflectionless topological negative or positive refraction occurs at different hinges, forming a closed loop around the corner or across the entire crystal. By adopting supercell modulation, we propose a general strategy to design 3D photonic Chern insulators with arbitrary Chern vectors [e.g., $\mathbf{C} = (2, 3, -6)$] featuring multiple arbitrarily large Chern numbers and oriented along arbitrary directions, resulting in multimodal chiral surface state transport and torus knot or link surface states on a single crystal surface rather than at the interface between two 3D photonic Chern insulators with perpendicular Chern vectors.

RESULTS

3D photonic Chern insulator with a multicomponent Chern vector $\mathbf{C} = (1, 1, -1)$

To realize a 3D photonic Chern insulator with a multicomponent Chern vector $\mathbf{C} = (1, 1, -1)$, we start from a tilted 3D Haldane model (see sections S1 and S2 for the standard and tilted 3D Haldane models), which contains two different types of sites having on-site energies of $+M$ and $-M$, respectively, and coupled with nearest-neighbor (NN) real coupling t_1 (yellow solid lines) and next–nearest-neighbor (NNN) complex coupling $t_2 e^{i\phi}$ (red and blue arrow lines). The NNN

[1]School of Electrical Engineering and Intelligentization, Dongguan University of Technology, Dongguan 523808, China. [2]State Key Laboratory of Optical Fiber and Cable Manufacture Technology, Department of Electronic and Electrical Engineering, Guangdong Key Laboratory of Integrated Optoelectronics Intellisense, Southern University of Science and Technology, Shenzhen 518055, China. [3]College of Aerospace Engineering, Chongqing University, Chongqing 400030, China. [4]Hubei Province Key Laboratory of Systems Science in Metallurgical Process, and College of Science, Wuhan University of Science and Technology, Wuhan 430081, China. [5]Research Center for Industries of the Future, School of Engineering, Westlake University, Hangzhou 310030, China. [6]Department of Electronic Engineering, The Chinese University of Hong Kong, Hong Kong SAR, China.
*Corresponding author. Email: gaoz@sustech.edu.cn
†These authors contributed equally to this work.

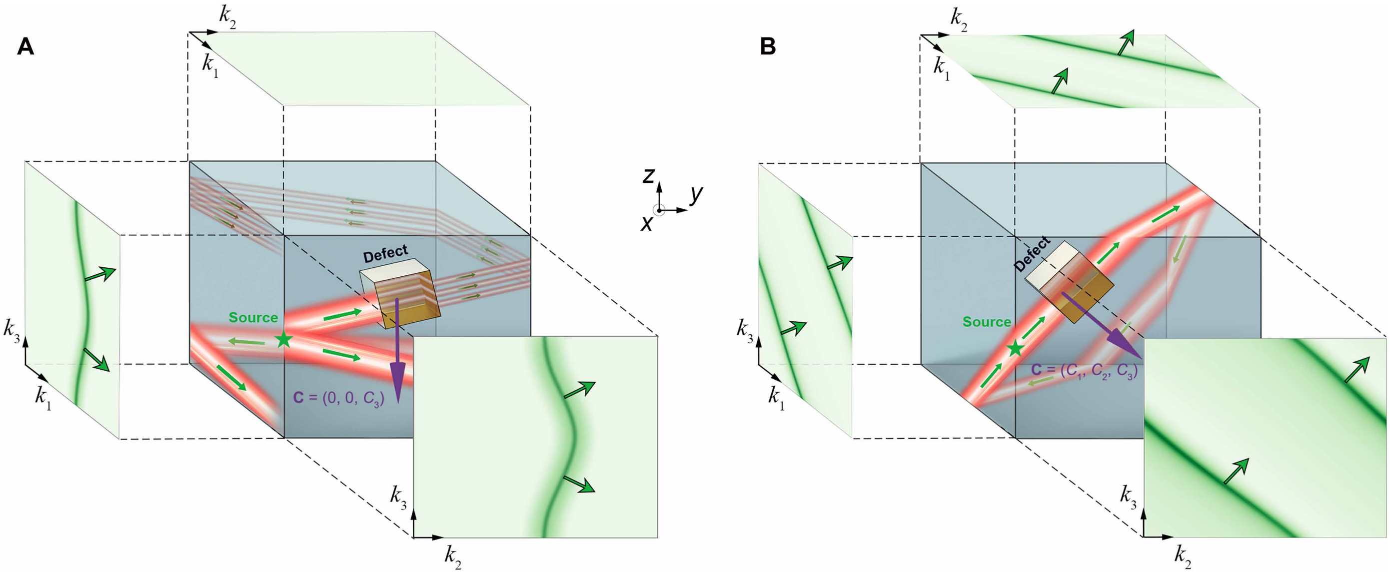

Fig. 1. 3D photonic Chern insulators with the simplest form of Chern vectors C = (0, 0, C_3) and arbitrary Chern vectors C = (C_1, C_2, C_3). (**A** and **B**) Schematic of chiral surface state (red color) propagating on the surfaces of 3D photonic Chern insulators with (A) the simplest form of Chern vectors **C** = (0, 0, C_3) having a single nonzero component and (B) arbitrary Chern vectors **C** = (C_1, C_2, C_3) having multiple nonzero components. The green star represents the point source, and the purple arrow represents the Chern vector. The green arrows indicate the propagation direction and amplitude of the chiral surface states. The yellow block represents the metallic defect. The six green planes represent the isofrequency contours of the $(0\bar{1}0)$, (100), and (001) surfaces, with those in (B) being reproduced from the isofrequency contours in Fig. 2 (M to O) for conceptual illustration.

couplings exist both within the same layer and between adjacent layers, and four NN couplings (black dashed lines) are replaced by two slanted interlayer couplings (yellow solid lines) between different sublattice sites in adjacent layers. The interlayer couplings between the two sublattice sites are t_a and t_b (red and blue solid lines), respectively. The Bloch Hamiltonian of the tilted 3D Haldane model is given by $H(k) = \begin{pmatrix} \Delta^+ & \Phi^- \\ \Phi^+ & \Delta^- \end{pmatrix}$, where $\Delta^\pm = \pm M + 2t_{a,b}\cos k_3 + \Theta^\pm(t_2, \phi)$ with $\Theta^\pm(t_2, \xi) = 2t\left[\cos(\xi \pm k_1 \pm k_3) + \cos(\xi \mp k_2 \mp k_3) + \cos(\xi \mp k_1 \mp k_2)\right]$ and $\Phi^\pm = t_1\left[e^{\mp ik_3} + e^{\pm ik_1} + e^{\pm ik_2}\right]$. The tilted 3D Haldane model yields a nontrivial bandgap characterized by a multicomponent Chern vector $\mathbf{C} = (1, 1, -1)$. Consequently, the resulting chiral surface states can reside on all six surfaces of a finite sample, enabling genuine robust chiral transport along arbitrary directions.

The 3D tight-binding model can be implemented in a tilted 3D gyromagnetic photonic crystal, as shown in Fig. 2A. Figure 2B presents the unit cell of the tilted 3D gyromagnetic photonic crystal, which consists of a gyromagnetic rod (red color) sandwiched between two permanent magnets (gray color) and mounted on a tilted metallic plate (yellow color). The top and the side views of the tilted metallic plate are shown in Fig. 2 (C and D), respectively. The metallic plate in the top view (Fig. 2C) forms a hexagonal unit cell, with its six corners perforated with identical air holes to introduce interlayer couplings. In the side view (Fig. 2D), the flat (tilted) segment of the metallic plate introduces in-plane intralayer (out-of-plane interlayer) NN couplings. To engineer the tilted NNN complex couplings, we rotated the gyromagnetic rod by an angle β about the x axis and then by an angle α about the z axis, starting from its initial z direction. In this case, the body-fixed coordinate system of the rod (denoted as XYZ), originally aligned with the global coordinate system xyz, can be obtained by intrinsic Z-X-Z rotations defined by three Euler angles α, β, and 0, as shown in Fig. 2E. As a result, the 3D tilted gyromagnetic photonic crystal features a tilted effective magnetic field $\mathbf{B}_{\text{eff}}$ that enables nonreciprocity along each primitive lattice vector a_i ($i = 1, 2, 3$). In stark contrast, in the previous 3D photonic Chern insulator with a Chern vector $\mathbf{C} = (0, 0, -1)$, the effective magnetic field $\mathbf{B}_{\text{eff}}$ is parallel to the z axis, and thus the nonreciprocity is restricted to the xy plane, that is, there exists no nonreciprocity along the z direction.

The 3D tilted gyromagnetic photonic crystal has a complete 3D photonic bandgap (green region) ranging from 13.4 to 14.9 GHz, as shown in Fig. 2F. We then characterize the topological invariant of the photonic bandgap using the Wilson loop approach, revealing a Chern vector $\mathbf{C} = (1, 1, -1)$ with all components being nonzero (see section S3 for details). Compared with the Chern vector $\mathbf{C} = (0, 0, -1)$, this Chern vector with multiple nonzero components guarantees the existence of genuine chiral surface states on all surfaces of a finite 3D Chern crystal, as shown in Fig. 2 (G to I), in which the red, blue, and yellow sheets represent the chiral surface states on $(0\bar{1}0)$, $(\bar{1}00)$, and (001) surfaces, respectively. To further demonstrate the genuine nonreciprocal transport of the chiral surface states along arbitrary directions, we plot their dispersions with one of the wave vectors fixed (Fig. 2, J to L) and isofrequency contours at 14.3 GHz (Fig. 2, M to O) for the $(0\bar{1}0)$, $(\bar{1}00)$, and (001) surfaces, respectively. For the $(0\bar{1}0)$ surface, the chiral surface state dispersions (Fig. 2J) exhibit positive group velocities along both the $+k_1$ and $+k_3$ directions, indicating the chiral surface states propagate nonreciprocal along the [101] diagonal direction, consistent with the isofrequency contour as shown in Fig. 2M. Moreover, because of the nonzero Chern vector components $C_1 = 1$ and $C_3 = -1$, the Fermi loop winds once

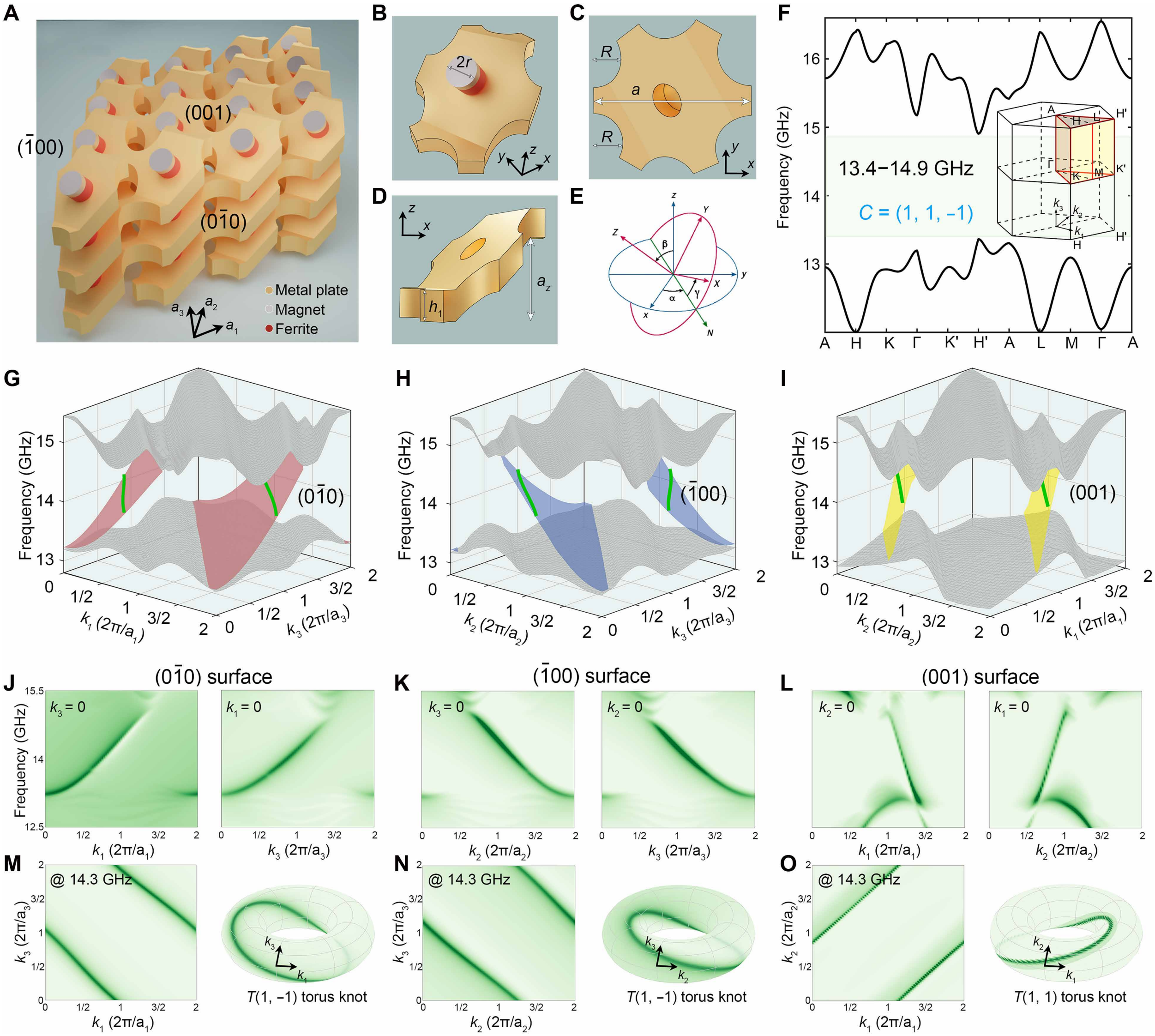

Fig. 2. Design of a 3D photonic Chern insulator with a multicomponent Chern vector C = (1, 1, −1) in a tilted gyromagnetic photonic crystal. (**A**) Schematic view of the 3D photonic Chern insulator with a Chern vector **C** = (1, 1, −1). (**B**) A unit cell of the 3D tilted gyromagnetic photonic crystal consisting of a gyromagnetic rod (red cylinder) sandwiched between two permanent magnets (gray cylinders) and inserted into a blind air hole on a tilted metallic plate (yellow region). (**C** and **D**) Top (C) and side (D) views of the tilted metallic plate. (**E**) The rotating coordinate system is established for the tilted gyromagnetic rods. The lattice constants in the *xy* plane and *z* direction are $a = 13$ mm and $a_z = 7.14$ mm, and the other geometrical parameters are $r = 1.7$ mm, $h_1 = 3$ mm, $\alpha = -60°$, $\beta = 43.57$nd the $R = 3$ mm, respectively. (**F**) Calculated bulk band structure of the 3D tilted gyromagnetic photonic crystal along the high-symmetry lines of 3D Brillouin zone (BZ) (inset). (**G** to **I**) Simulated chiral surface state dispersions (red, blue, and yellow sheets) for the $(0\bar{1}0)$ (G), $(\bar{1}00)$ (H), and (001) surfaces (I), respectively. (**J** to **O**) Calculated frequency-dependent surface dispersions (top panels) and isofrequency contours at 14.3 GHz (bottom panels) for $(0\bar{1}0)$ [(J) and (M)], $(\bar{1}00)$ [(K) and (N)], and (001) [(L) and (O)] surfaces, respectively. The isofrequency contours are reproduced in Fig. 1B for conceptual illustration.

along the $+k_1$ and $-k_3$ directions, respectively, forming a $T(1, -1)$ torus knot in the surface Brillouin zone (SBZ), as shown in the right panel of Fig. 2M. In contrast with the previous Chern vectors having a single nonzero component, the Chern vectors with multiple nonzero components guarantee the genuine nonreciprocal transport of chiral surface states along arbitrary directions with enhanced robustness (see fig. S5 for details). To our best knowledge, these genuine chiral surface states with 2D nonreciprocity have never been reported in any photonic system. Likewise, the chiral surface states on the $(\bar{1}00)$ and (001) surfaces exhibit similar properties.

Experimental realization of a 3D photonic Chern insulator with a multicomponent Chern vector C = (1, 1, −1)

Now, we experimentally demonstrate the 3D photonic Chern insulator with a multicomponent Chern vector **C** = (1, 1, −1). The experimental sample is illustrated in Fig. 3A and comprises 38 layers of tilted metallic plates and gyromagnetic rods sandwiched between permanent magnets (see fig. S6 for details). We design a tenon-and-mortise structure at the top and bottom of the metallic claddings to fix the tilted metallic plates. To see the internal structure of the 3D tilted gyromagnetic photonic crystal, we separate the sample into

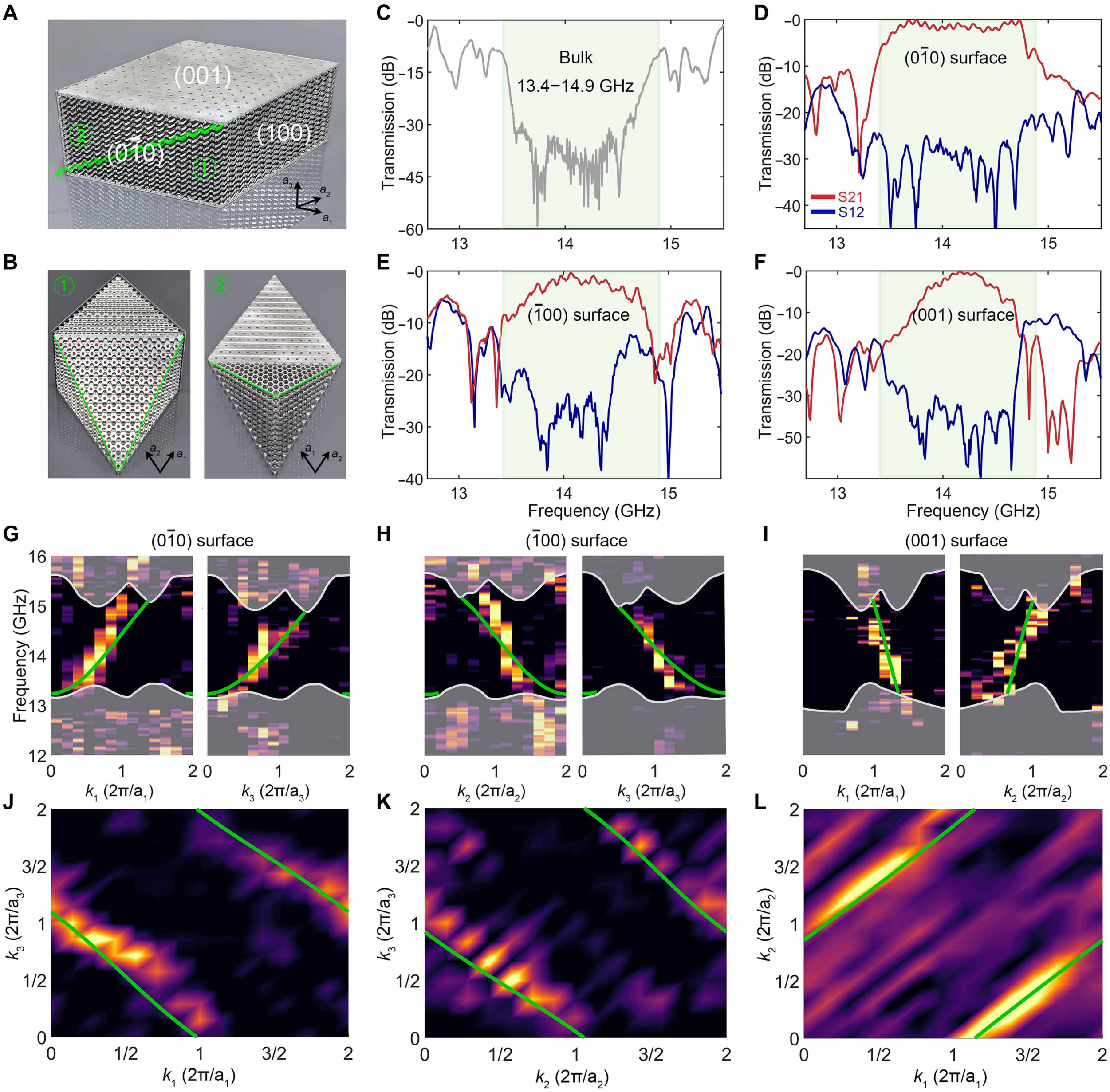

Fig. 3. Experimental realization of a 3D photonic Chern insulator with a Chern vector C = (1, 1, −1). (**A**) Photograph of the fabricated experimental sample. (**B**) The internal structure of the experimental sample is illustrated by separating it into two parts along the green line in (A). (**C**) Measured bulk transmission spectrum of the 3D photonic Chern insulator. (**D** to **F**) Measured forward (S21 marked by red line) and backward (S12 marked by blue line) transmission spectra of the chiral surface states on the $(0\bar{1}0)$ (D), $(\bar{1}00)$ (E), and (001) (F) surfaces, respectively. (**G** to **L**) Measured (color maps) and simulated (green lines) frequency-dependent surface dispersions and surface isofrequency contours at 14.3 GHz on the $(0\bar{1}0)$ (G and J), $(\bar{1}00)$ [(H) and (K)], and (001) [(I) and (L)] surfaces, respectively.

two parts (marked as ① and ②) along the green line in Fig. 3A, as shown in Fig. 3B.

We first measure the bulk transmission spectrum of the crystal, as shown in Fig. 3C, from which we can observe a wide transmission dip corresponding to the 3D photonic bandgap (green region). We then measure the transmission spectra of the chiral surface states on $(0\bar{1}0)$, $(\bar{1}00)$, and (001) surfaces, as shown in Fig. 3 (D to F), respectively, from which we can observe that the forward transmission (S21; red line) is much larger than the backward transmission (S12; blue line) within the photonic bandgap (green region), verifying the nonreciprocal transmission of the chiral surface states on all surfaces. Figure 3 (G to I and J to L) shows the measured (color maps) and simulated (green lines) frequency-dependent surface dispersions and isofrequency contours at 14.3 GHz on $(0\bar{1}0)$, $(\bar{1}00)$, and (001) surfaces, respectively, from which we can observe that, for each surface, the projected bulk bands (white regions) are gapped with chiral surface states spanning the entire photonic bandgap. The topological surface states exhibit positive or negative group velocities in two distinct wave-vector directions on each surface, further confirming the existence of genuine chiral surface states on all surfaces and their 2D nonreciprocity along arbitrary directions.

Because the chiral surface states can propagate on all six surfaces, we now explore what will happen when the chiral surface states cross the hinges separating different surfaces. We first place a point source (green star) at the center of the 60° hinge to excite the chiral surface states and use another point probe to map their electric field distributions. As shown in Fig. 4A, the self-collimated chiral surface states propagate nonreciprocally (green arrows) across three adjacent surfaces around the corner, and reflectionless topological negative refractions occur at the hinges, matching well with the simulation results shown in Fig. 4B. We then place the point source (green star) at the center of 120° hinge and repeat the electric field mapping measurements. As shown in Fig. 4C, the chiral surface states propagate nonreciprocally across all six surfaces, and reflectionless topological positive refractions occur at the hinges, in agreement with the simulation results shown in Fig. 4D. These unique phenomena can be well explained by the surface isofrequency contour analysis on two adjacent surfaces (see section S4 for details). We then examine the robustness of the chiral surface states by positioning a metallic obstacle (inset in Fig. 4E) in the path of the chiral surface states on the $(\bar{1}00)$ surface. As shown in Fig. 4E, the chiral surface state propagates smoothly around the metallic obstacle without any backscattering, and its measured electric field distribution remains almost the same as that of a perfect sample without an obstacle, as shown in Fig. 4F.

3D photonic Chern insulators with arbitrary Chern vectors

Last, we demonstrate how 3D photonic Chern insulators with arbitrary Chern vectors can be realized through supercell modulation. Figure 5A shows the supercell modulation configuration for an arbitrary Chern vector **C** = (2, 3, −6). The supercell comprises two and three tilted unit cells along the a_1 and a_2 axes, respectively, and six unit cells along the a_3 axis. To make the supercell act as a new irreducible primitive unit cell along each lattice vector a_i ($i = 1, 2, 3$), we first modulate the perforated air holes with different radii (blue and red circles), and then we swap the blue and red air holes in the third layer (red frame marked as 2), as illustrated in Fig. 5A. As a result, this supercell structure represents a unit cell of a 3D photonic Chern insulator with a large Chern vector **C** = (2, 3, −6), whose component's absolute value exactly equals to the number of original unit cells (Fig. 2B) along each axis and component's signs are determined by the magnetic field direction, providing a general strategy to design 3D photonic Chern insulators with arbitrary Chern vectors.

To investigate the topological properties of the 3D photonic Chern insulator with an arbitrary Chern vector **C** = (2, 3, −6), we simulate its bulk band structure, frequency-dependent surface dispersions, and surface isofrequency contour at 14.1 GHz for the $(0\bar{1}0)$, $(\bar{1}00)$, and (001) surfaces, respectively, as shown in Fig. 5 (B to H). The bulk band structure (Fig. 5B) has a complete 3D photonic bandgap ranging from 13.4 to 14.9 GHz with a Chern vector **C** = (2, 3, −6), and the frequency-dependent surface dispersions (Fig. 5, C to E) reveal that multiple chiral surface states coexist on each surface, with their number equal to the components of the Chern vector parallel to each surface, respectively. For instance, for the $(0\bar{1}0)$ surface, the number of chiral surface states is six and two along the $+k_1$ and $+k_3$ directions, respectively, because $C_1 = 2$ and $C_3 = -6$.

We now study the winding behaviors of the arbitrary Chern vector **C** = (2, 3, −6) with multiple large, nonzero components. According

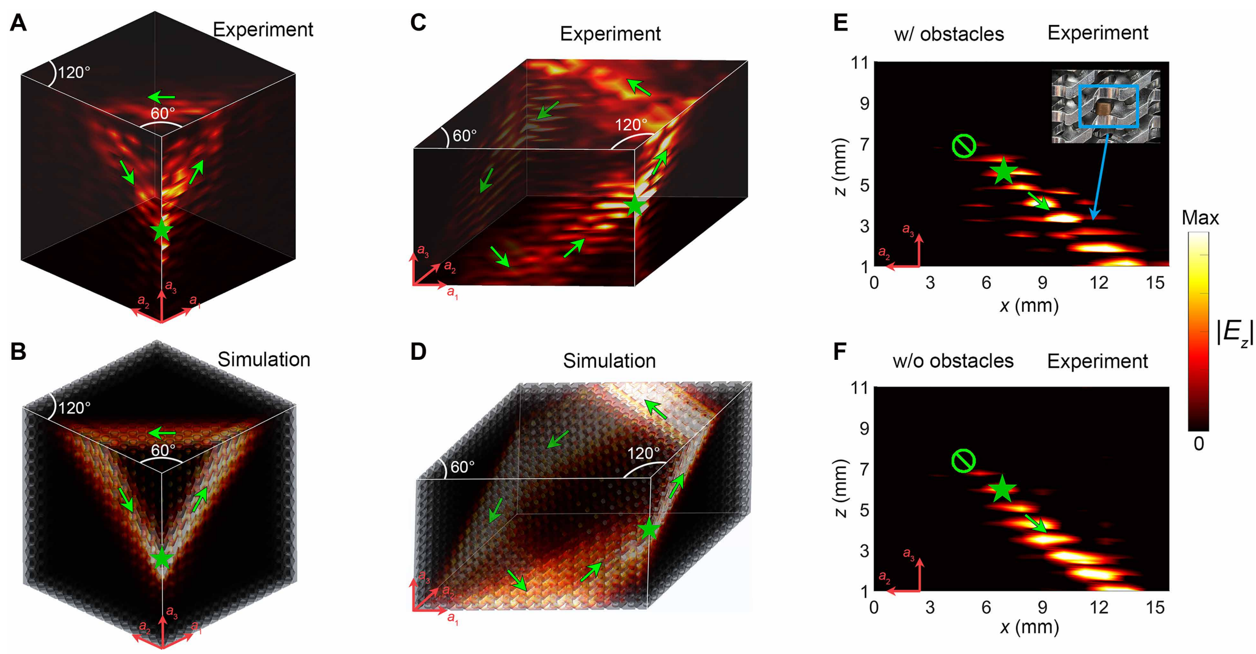

Fig. 4. Nonreciprocal topological negative and positive refraction and robustness of the genuine chiral surface states. (**A** and **B**) Measured (A) and simulated (B) electric field distributions of the nonreciprocal and reflectionless topological negative refraction of chiral surface states around the 60° corner. The green star represents the point source, and the green arrows indicate the propagation path of the chiral surface states. (**C** and **D**) Measured (C) and simulated (D) electric field distributions of the nonreciprocal and reflectionless topological positive refraction of chiral surface states across the entire crystal. The simulated electric field distributions in (B) and (D) are reproduced in fig. S4 to maintain a clear link between the main text and the Supplementary Materials. (**E** and **F**) Measured electric field distributions of chiral surface states on the $(\bar{1}00)$ surface (E) with and (F) without a metallic obstacle. The inset shows the photo of the metallic obstacle. w, with; w/o, without.

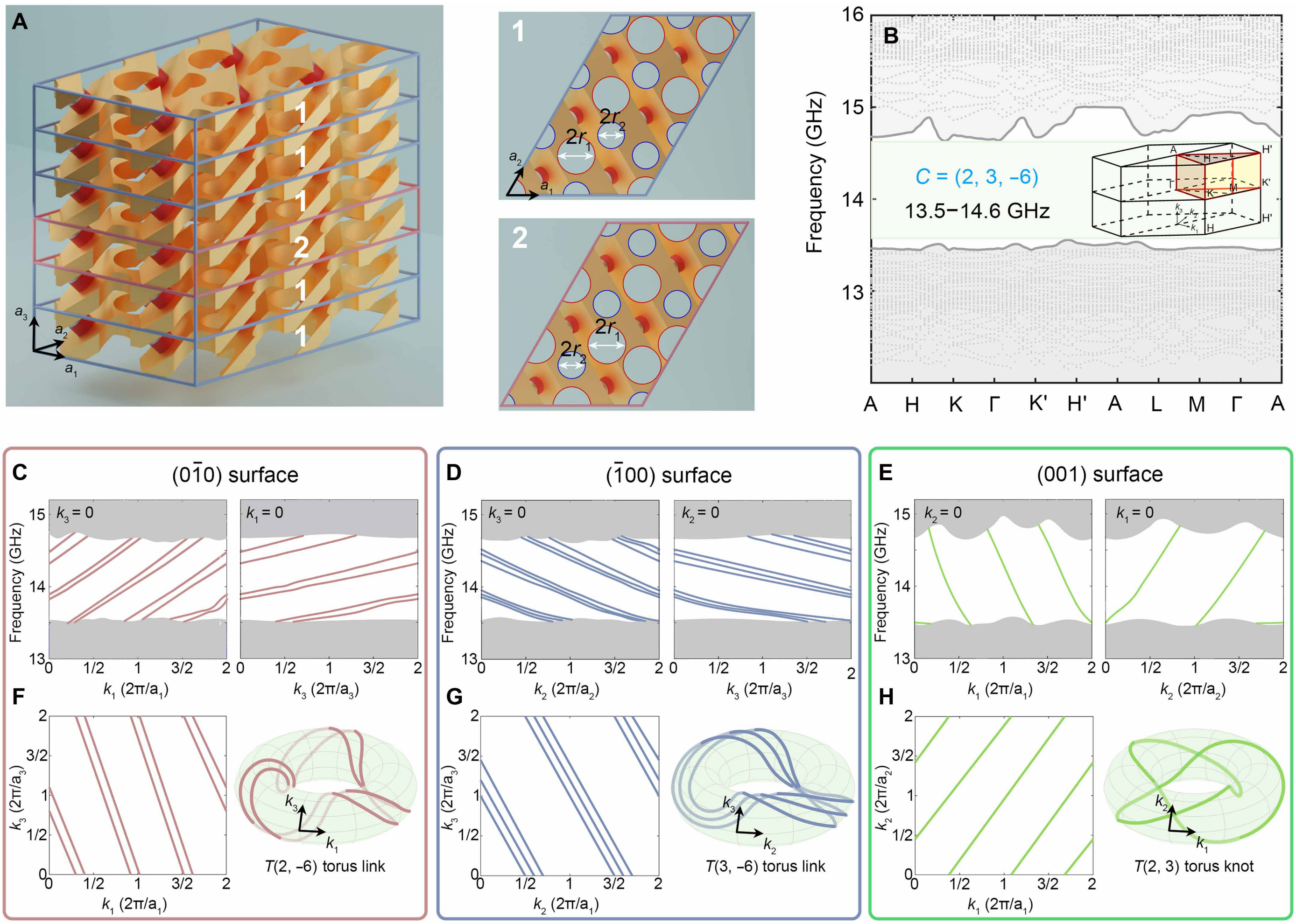

Fig. 5. 3D photonic Chern insulator with an arbitrary Chern vector C = (2, 3, −6). (**A**) Schematic view of a 2 by 3 by 6 supercell of a 3D photonic Chern insulator. The right panels show top views of the tilted metallic plates with perforated air holes, with radii $r_1 = 3.5$ mm and $r_2 = 2.5$ mm, in the layers marked 1 and 2. (**B**) Calculated bulk band structure of the 3D photonic Chern insulator with an arbitrary Chern vector **C** = (2, 3, −6) along high-symmetry lines of 3D BZ (inset). The green region represents the 3D complete photonic bandgap. (**C** to **E**) Simulated frequency-dependent surface dispersions. (**F** to **H**) Isofrequency contours at 14.1 GHz and winding behaviors of the Fermi loops on the $(0\bar{1}0)$, $(\bar{1}00)$, and (001) surfaces, respectively.

to the knot theory (*34*), the fermi loop on the $(0\bar{1}0)$ surface forms a $T(2, -6)$ torus link, which consists of two interlinked $T(1, -3)$ torus knots winding 1 cycle along k_1 and 3 cycles along k_3 with opposite directions because the Chern vector components $C_1 = 2$ and $C_3 = -6$ are not coprime, as shown in the right panel of Fig. 5F. Similarly, the Fermi loop on the $(\bar{1}00)$ surface forms a $T(3, -6)$ torus link, composing of three interlinked $T(1, -2)$ torus knots winding 1 cycle along k_1 and 2 cycles along k_3 with opposite directions, as shown in the right panel of Fig. 5G. In contrast, the situation is different for the (001) surface, as shown in the right panel of Fig. 5H, the Fermi loop forms a single T (2, 3) torus knot because $C_1 = 2$ and $C_3 = 3$. These torus knots or torus links are formed on the surfaces of a single 3D photonic Chern insulator with arbitrary Chern vectors, in contrast to the previously reported torus links or Hopf links formed at the interface between two 3D Chern insulators with perpendicular Chern vectors, which have only a single nonzero component (*22*).

DISCUSSION

In conclusion, we have experimentally demonstrated a 3D photonic Chern insulator with a Chern vector **C** = (1, 1, −1) having multiple nonzero components in a tilted gyromagnetic photonic crystal. In contrast to the previously reported 3D photonic Chern insulator with a Chern vector **C** = (0, 0, −1) having only a single nonzero component (*22*), we show that the 3D photonic Chern insulators with Chern vectors having multiple nonzero components exhibit some unique properties, including chiral surface states on all six surfaces, genuine chiral surface transport with 2D nonreciprocity and enhanced robustness, nonreciprocal and reflectionless topological negative or positive refractions at the hinges. We establish a general strategy for constructing 3D photonic Chern insulators with arbitrarily large Chern vectors, which support exotic torus knot or link states on the surfaces of a single crystal, rather than at the interface between two Chern insulators with perpendicular Chern vectors. Although the current implementation is demonstrated in the microwave regime, the underlying design principles are inherently scalable to higher frequencies—including the terahertz and optical domains—through the use of optical nonlinearities (*35*) or gyrotropic materials (*19*, *36*). Our work provides a comprehensive understanding of the topological Chern vectors underlying the Chern-type bulk-edge correspondence and may inspire research on the 3D quantum Hall effect (*33*) and other bosonic systems, such as phonons, magnons, and polaritons.

MATERIALS AND METHODS

Numerical simulations

All numerical results presented in this work are calculated with a finite-element–method software (COMSOL Multiphysics RF module). The bulk band structures are simulated using a hexagonal unit cell with periodic boundary conditions in all directions. The frequency-dependent dispersions of the chiral surface states on $(0\bar{1}0)$, $(\bar{1}00)$, and (001) surfaces are calculated using $1 \times 15 \times 1$, $15 \times 1 \times 1$, and $1 \times 1 \times 15$ supercells, respectively. When the external magnetic field is rotated about the x axis by an angle β and then an angle α about the z axis, the relative permeability tensor of the gyromagnetic materials has the form $[\mu_r] = \begin{bmatrix} \mu_{xx} & \mu_{xy} & \mu_{xz} \\ \mu_{yx} & \mu_{yy} & \mu_{yz} \\ \mu_{zx} & \mu_{zy} & \mu_{zz} \end{bmatrix}$, where $\mu_{xx} = \mu_m \cos^2\alpha + (\mu_m \cos^2\beta + \sin^2\beta)\sin^2\alpha$, $\mu_{xy} = j\mu_k \cos\beta - (-1+\mu_m)\cos\alpha \sin^2\beta \sin\alpha$, $\mu_{xz} = \sin\beta(-j\mu_k \cos\alpha - (-1+\mu_m)\cos\beta \sin\alpha)$, $\mu_{yx} = -j\mu_k \cos\beta - (-1+\mu_m)\cos\alpha \sin^2\beta \sin\alpha$, $\mu_{yy} = \cos^2\alpha(\mu_m \cos^2\beta + \sin^2\beta) + \mu_m \sin^2\alpha$, $\mu_{yz} = \sin\beta(-(-1+\mu_m)\cos\beta \cos\alpha + j\mu_k \sin\alpha)$, $\mu_{zx} = \sin\beta(j\mu_k \cos\alpha - (-1+\mu_m)\cos\beta \sin\alpha)$, $\mu_{zy} = -\sin\beta((-1+\mu_m)\cos\beta\cos\alpha + j\mu_k \sin\alpha)$, $\mu_{zz} = \cos^2\beta + \mu_m \sin^2\beta$, $\mu_m = 1 + \omega_m(\omega_0 + i\alpha\omega)/[(\omega_0 + i\alpha\omega)^2 - \omega^2]$, $\mu_k = \omega_m \omega/[(\omega_0 + i\alpha\omega)^2 - \omega^2]$, $\omega_m = \mu_0 \gamma M_s$, $\omega_0 = \gamma \mu_0 H_0$, and $\mu_0 H_0$ is the external magnetic field, $\gamma = 1.759 \times 10^{11}$ C/kg is the gyromagnetic ratio, $\alpha = 0.0088$ is the damping coefficient, and ω is the operating frequency. Under an external magnetic field of 0.26 tesla, the dispersions of the permeability tensor elements μ_m and μ_k are shown in fig. S7, from which we can see that the resonance frequency of the permeability is far from the operating frequency range of the chiral surface states. Therefore, the dispersion of the permeability of the gyromagnetic materials is rather weak within the frequency range of interest.

Materials and experimental setups

In the experiment, we use commercially available yttrium-iron-garnet (YIG) ferrites as gyromagnetic materials to break the time-reversal symmetry. The radius and height of the YIG ferrites are 1.7 and 2 mm, respectively. The YIG ferrites have a saturation magnetization of M_s = 1780 G. Its permittivity is approximately $\varepsilon_r = 14.3 + 0.0002i$, which remains essentially constant at microwave frequencies. The permanent magnets (Sm2Co17) are electroplated with 0.002 mm of nickel. One pair of magnets provides an overall uniform external magnetic field of about 0.26 tesla to magnetize the gyromagnetic rods. The 38 layers of perforated metallic plates are fabricated using the laser-cutting technique (see details in fig. S6). The ordinal numbers correspond to the layers stacked sequentially during the assembly process. To secure the inclined angle, these metallic plates are inserted into the surrounding metallic cladding via a mortise-and-tenon joint. The gyromagnetic rods sandwiched between two permanent magnets are inserted into the blind air holes of the perforated metallic plates. In the experimental measurements, two microwave dipole antennas, functioning as the source and probe, are connected to a vector network analyzer (Keysight E5080). The complex electric field distributions are mapped by inserting the probe into the air holes one by one and scanning along the z direction in small steps. Then, the 2D Fourier transformation was applied to the measured complex electric field distributions at each frequency to obtain the measured surface dispersion relations.

Supplementary Materials

This PDF file includes:
Supplementary Text
Figs. S1 to S7

REFERENCES

1. S. Raghu, F. D. M. Haldane, Analogs of quantum-Hall-effect edge states in photonic crystals. *Phys. Rev. A* **78**, 033834 (2008).
2. F. D. M. Haldane, S. Raghu, Possible realization of directional optical waveguides in photonic crystals with broken time-reversal symmetry. *Phys. Rev. Lett.* **100**, 013904 (2008).
3. Z. Wang, Y. Chong, J. D. Joannopoulos, M. Soljačić, Observation of unidirectional backscattering-immune topological electromagnetic states. *Nature* **461**, 772–775 (2009).
4. Z. Wang, Y. D. Chong, J. D. Joannopoulos, M. Soljačić, Reflection-free one-way edge modes in a gyromagnetic photonic crystal. *Phys. Rev. Lett.* **100**, 013905 (2008).
5. Y. Poo, R.-X. Wu, Z. Lin, Y. Yang, C. T. Chan, Experimental realization of self-guiding unidirectional electromagnetic edge states. *Phys. Rev. Lett.* **106**, 093903 (2011).
6. S. A. Skirlo, L. Lu, Y. Igarashi, Q. Yan, J. Joannopoulos, M. Soljačić, Experimental observation of large Chern numbers in photonic crystals. *Phys. Rev. Lett.* **115**, 253901 (2015).
7. X. Ni, D. Purtseladze, D. A. Smirnova, A. Slobozhanyuk, A. Alù, A. B. Khanikaev, Spin- and valley-polarized one-way Klein tunneling in photonic topological insulators. *Sci. Adv.* **4**, eaap8802 (2018).
8. P. Zhou, G.-G. Liu, Y. Yang, Y.-H. Hu, S. Ma, H. Xue, Q. Wang, L. Deng, B. Zhang, Observation of photonic antichiral edge states. *Phys. Rev. Lett.* **125**, 263603 (2020).
9. M. Wang, R. Zhang, L. Zhang, D. Wang, Q. Guo, Z. Zhang, C. T. Chan, Topological one-way large-area waveguide states in magnetic photonic crystals. *Phys. Rev. Lett.* **126**, 067401 (2021).
10. J. Chen, Z. Li, Prediction and observation of robust one-way bulk states in a gyromagnetic photonic crystal. *Phys. Rev. Lett.* **128**, 257401 (2022).
11. J. Chen, Y. Zheng, S. Yang, F. Shi, Z. Y. Li, C. W. Qiu, One-way valley-robust transport in edge-tailored photonic crystals. *Phys. Rev. Lett.* **134**, 203803 (2025).
12. J. Chen, Y. Zheng, S. Yang, A. Alù, Z. Y. Li, C. W. Qiu, Chern-protected flatband edge state in metaphotonics. *Phys. Rev. Lett.* **134**, 223806 (2025).
13. F. F. Li, H. X. Wang, Z. Xiong, Q. Lou, P. Chen, R. X. Wu, Y. Poo, J. H. Jiang, S. John, Topological light-trapping on a dislocation. *Nat. Commun.* **9**, 2462 (2018).
14. G. G. Liu, S. Mandal, P. Zhou, X. Xi, R. Banerjee, Y. H. Hu, M. Wei, M. Wang, Q. Wang, Z. Gao, H. Chen, Y. Yang, Y. Chong, B. Zhang, Localization of chiral edge states by the non-Hermitian skin effect. *Phys. Rev. Lett.* **132**, 113802 (2024).
15. L. He, Z. Addison, E. J. Mele, B. Zhen, Quadrupole topological photonic crystals. *Nat. Commun.* **11**, 3119 (2020).
16. P. Zhou, G. G. Liu, Z. Wang, S. Li, Q. Xie, Y. Zhang, S. Mandal, X. Xi, Z. Gao, L. Deng, B. Zhang, Realization of a quadrupole topological insulator phase in a gyromagnetic photonic crystal. *Natl. Sci. Rev.* **11**, nwae121 (2024).
17. S. Mandal, Z. Wang, G. G. Liu, H. T. Teo, R. Banerjee, P. Zhou, X. Xi, Z. Gao, B. Zhang, Photonic bilayer Chern insulator with corner states. *Phys. Rev. Lett.* **135**, 016903 (2025).
18. G. Wang, L. Lu, Topological microwave isolator with >100-dB isolation. *Nat. Photonics* **19**, 1064–1069 (2025).
19. B. Bahari, A. Ndao, F. Vallini, A. E. Amili, Y. Fainman, B. Kanté, Nonreciprocal lasing in topological cavities of arbitrary geometries. *Science* **358**, 636–640 (2017).
20. L. Lu, H. Gao, Z. Wang, Topological one-way fiber of second Chern number. *Nat. Commun.* **9**, 5384 (2018).
21. C. Devescovi, M. García-Díez, I. Robredo, M. Blanco de Paz, J. Lasa-Alonso, B. Bradlyn, J. L. Mañes, M. G. Vergniory, A. García-Etxarri, Cubic 3D Chern photonic insulators with orientable large Chern vectors. *Nat. Commun.* **12**, 7330 (2021).
22. G. G. Liu, Z. Gao, Q. Wang, X. Xi, Y. H. Hu, M. R. Wang, C. Q. Liu, X. Lin, L. J. Deng, S. A. Yang, P. H. Zhou, Y. Yang, Y. D. Chong, B. Zhang, Topological Chern vectors in three-dimensional photonic crystals. *Nature* **609**, 925–930 (2022).

23. X. Xi, B. Yan, L. Yang, Y. Meng, Z. Zhu, J. M. Chen, Z. Wang, P. Zhou, Y. Yang, H. Chen, G. G. Liu, B. Zhang, Z. Gao, Topological antichiral surface states in a magnetic Weyl photonic crystal. *Nat. Commun.* **14**, 1991 (2023).
24. C. Devescovi, A. Morales-Pérez, Y. Hwang, M. García-Díez, I. Robredo, J. Mañes, B. Bradlyn, A. García-Etxarri, M. Vergniory, Axion topology in photonic crystal domain walls. *Nat. Commun.* **15**, 6814 (2024).
25. H.-S. Lai, Y.-C. Zhou, Z.-Q. Sun, C. He, Y.-F. Chen, Photonic axion insulator with non-coplanar chiral hinge transport. *Nat. Commun.* **16**, 3826 (2025).
26. G. G. Liu, S. Mandal, X. Xi, Q. Wang, C. Devescovi, A. Morales-Pérez, Z. Wang, L. Yang, R. Banerjee, Y. Long, Y. Meng, P. Zhou, Z. Gao, Y. Chong, A. García-Etxarri, M. G. Vergniory, B. Zhang, Photonic axion insulators. *Science* **378**, 162–166 (2025).
27. F. Chen, N. Han, S. Pu, R. Zhao, L. Zhang, Q. Chen, Y. Hu, M. Tong, W. Li, J. Wu, Y. Ren, X. Li, W. Yin, H. Chen, R. X. Zhang, Y. Yang, Photonic antiferromagnetic topological insulator with a single surface Dirac cone. *Sci. Adv.* **11**, eadu6230 (2025).
28. H. Xia, J. Li, S. Yuan, M. Xiao, Photonic realization of chiral hinge states in a Chern-insulator stack. *Phys. Rev. B* **111**, L041112 (2025).
29. Z. Li, S. Ma, S. Li, O. You, Y. Liu, Q. Yang, Y. Xiang, P. Zhou, S. Zhang, Observation of copropagating chiral zero modes in magnetic photonic crystals. *Phys. Rev. Lett.* **134**, 033802 (2025).
30. M. Wang, R. Zhang, C. Zhang, H. Xue, H. Jia, J. Hu, D. Wang, T. Jiang, C. Chan, Three-dimensional nonreciprocal transport in photonic topological heterostructure of arbitrary shape. *Sci. Adv.* **11**, eadq9285 (2025).
31. L. Yang, X. Xi, Y. Meng, Z. Zhu, Y. Wu, J. Chen, M. Cheng, K. Xiang, P. P. Shum, Y. Yang, H. Chen, J. Li, B. Yan, G. G. Liu, B. Zhang, Z. Gao, Three-dimensional acoustic Chern insulators with arbitrary Chern vectors. *Phys. Rev. Res.* **7**, 023280 (2025).
32. F. Y. Ma, J. R. Feng, F. Li, Y. Wu, D. Zhou, Floquet Chern vector topological insulators in three dimensions. *Phys. Rev. B* **111**, 134301 (2025).
33. Z. Q. Zhang, S. G. Cheng, H. F. Liu, H. L. Li, H. Jiang, X. C. Xie, Chern vector protected three-dimensional quantized Hall effect. arXiv:2501.14493 [cond-mat.mes-hall] (2025).
34. V. Manturov, *Knot Theory* (CRC Press, ed. 2, 2018).
35. J. Jin, L. He, J. Lu, L. Chang, C. Shang, J. E. Bowers, E. J. Mele, B. Zhen, Towards Floquet Chern insulators of light. *Nat. Nanotechnol.* **20**, 1574–1579 (2025).
36. A. N. Grebenchukov, V. I. Ivanova, A. V. Suslov, G. I. Kropotov, M. K. Khodzitsky, Broadband terahertz isolator. *IEEE Trans. Terahertz Sci. Technol.* **12**, 81–86 (2022).

Acknowledgments
Funding: This work was funded by the National Key R&D Program under grant no. 2025YFA1412300 (to Z.G.); the National Natural Science Foundation of China under grant no. 62405053 (to X.X.), no. 62361166627 (to Z.G.), no. 62375118 (to Z.G.), no. 125B2093 (to Z.W.), no. 12304484 (to Y.M.), no. 12404053 (to Z.Z.), and no. 12502106 (to L.Y.); the Guangdong Basic and Applied Basic Research Foundation under grant no. 2025A1515012229 (to X.X.), no. 2024A1515012770 (to Z.G.), no. 2024A1515011371 (to Y.M.), and no. 2025A1515012284 (to Z.Z.); the Shenzhen Science and Technology Innovation Commission under grant no. 202308073000209 (to Z.G.); the High-level Special Funds under grant no. G03034K004 (to Z.G.); the Youth S&T Talent Support Programme of Guangdong Provincial Association for Science and Technology under grant no. SKXRC2025440 (to X.X.); the Research Grants Council of Hong Kong under grant no. N_CUHK479/23 (to X.S.); the Research Center for Industries of the Future at Westlake University under grant no. 210000006022312 (to G.-G.L.); the Westlake Education Foundation under grant no. 103110736022301 (to G.-G.L.); the Hubei Provincial Natural Science Foundation of China under grant no. 2025AFB011 (to B.Y.); and the Natural Science Foundation of Chongqing under grant no. CSTB2025NSCQ-GPX0776 (to L.Y.). **Author contributions:** Conceptualization: Z.G., G.-G.L., Y.M., and L.Y. Methodology: X.X., L.Y., Z.W., J.-M.C., Z.G., and Y.M. Software: X.X., Y.M., and L.Y. Validation: X.X., B.Y., Z.W., J.-M.C., T.X., Y.M., L.Y., G.-G.L., and Z.-X.Z. Formal analysis: X.X., B.Y., J.-M.C., Y.M., G.-G.L., M.-Q.C., L.Y., and Z.W. Investigation: X.X., Y.M., B.Y., M.-Q.C., Z.W., G.-G.L., and L.Y. Resources: X.X., Z.G., Y.M., G.-G.L., and L.Y. Data curation: X.X., B.Y., L.Y., and Y.M. Writing—original draft: X.X., L.Y., Y.M., and Z.G. Writing—review and editing: X.X., Z.G., J.-M.C., Y.M., G.-G.L., and L.Y. Visualization: X.X., Z.W., Z.Z., H.W., X.S., Z.G., Y.M., G.-G.L., and L.Y. Supervision: Z.G. and G.-G.L. Project administration: Z.G. and G.-G.L. Funding acquisition: Z.G., X.X., Z.W., X.S., Y.M., G.-G.L., and Z.-X.Z. **Competing interests:** The authors declare that they have no competing interests. **Data, code, and materials availability:** All data and code needed to evaluate and reproduce the results in the paper are present in the paper and/or the Supplementary Materials. This study did not generate new materials.

Submitted 14 January 2026
Accepted 29 May 2026
Published 8 July 2026
10.1126/sciadv.aef3784

Science Advances

Photonic arbitrary Chern vectors

Xiang Xi, Linyun Yang, Ziyao Wang, Bei Yan, Jing-Ming Chen, Yan Meng, Zhen-Xiao Zhu, Tao Xiao, Min-Qi Cheng, Zebin Zhu, Gui-Geng Liu, Hongcheng Wang, Xiankai Sun, and Zhen Gao

Sci. Adv. **12** (28), eaef3784. DOI: 10.1126/sciadv.aef3784

Science Advances (ISSN 2375-2548) is published by the American Association for the Advancement of Science. 1200 New York Avenue NW, Washington, DC 20005. The title *Science Advances* is a registered trademark of AAAS.